



Science Arts & Métiers (SAM)

is an open access repository that collects the work of Arts et Métiers Institute of Technology researchers and makes it freely available over the web where possible.

This is an author-deposited version published in: <https://sam.ensam.eu>
Handle ID: <http://hdl.handle.net/10985/17848>

To cite this version :

Stefania CHERUBINI, Emmanuel LERICHE, Jean-Christophe ROBINET, Jean-Christophe LOISEAU - Global Stability Analyses Unraveling Roughness-induced Transition Mechanisms - Procedia IUTAM - Vol. 14, p.182-191 - 2015

Any correspondence concerning this service should be sent to the repository

Administrator : scienceouverte@ensam.eu



Global stability analyses unraveling roughness-induced transition mechanisms

J.-Ch. Loiseau^{a,b,*}, J.-Ch. Robinet^a, S. Cherubini^a, E. Leriche^b

^a*DynFluid Laboratory, Arts et Métiers ParisTech, 151 Bd. de l'Hopital, 75013 Paris, France*

^b*Laboratoire de Mécanique de Lille, Avenue Paul Langevin, 59650 Villeneuve d'Ascq, France*

Abstract

The linear global instability and resulting transition to turbulence induced by a cylindrical roughness element of height h and diameter $d = 3h$ immersed within an incompressible boundary layer flow along a flat plate is investigated using the joint application of direct numerical simulations and three-dimensional stability analyses. The configuration investigated is the same as the one investigated experimentally by Fransson *et al.*¹⁰. Base flow computations show that the roughness element induces a wake composed of a central low-speed region surrounded by a three-dimensional shear layer and a pair of low- and high-speed streaks on each side. Results from the global stability analyses highlight the unstable nature of the central low-speed region and its crucial importance in the laminar-turbulent transition process. For the set of parameters considered, it is able to sustain a varicose global instability for which the predicted critical Reynolds number is only 6% larger than the one reported in Ref.10. A kinetic energy budget and wavemaker analysis revealed that this mode finds its root in the reversed flow region right downstream the roughness element and extracts most of its energy from the central low-speed region and streaks further downstream. Direct numerical simulations of the flow past this roughness element puts in the limelight the ability for this linear instability to give birth to hairpin vortices and thus trigger transition to turbulence.

Keywords:

Roughness-induced transition ; boundary layer ; global stability

1. Introduction

Delaying transition in spatially developing boundary layer flows has been a long time challenge. For small amplitude disturbances and supercritical Reynolds numbers, the linear stability theory predicts the slow transition process due to the generation, amplification and secondary instability of Tollmien-Schlichting (TS) waves. It has been shown recently in Ref.¹² that those TS waves can be stabilised by streamwise streaks. In this experimental work, sub-optimal streaks have been created using a periodic array of cylindrical roughness elements. Despite the stabilising effect of the streaks on the TS waves, the flow may undergo transition to turbulence right downstream the roughness elements

* Corresponding author. Tel.: +33-674-233-633 ; fax: +0-000-000-0000.

E-mail address: loiseau.jc@gmail.com

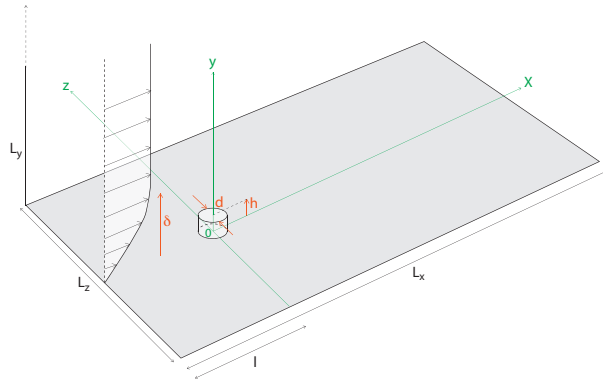


Fig. 1. Sketch of the computational domain considered. The parameters defining the roughness element's geometry take the following values: height $h = 1$ and diameter $d = 3$. The computational domain is characterised by $l = 15$ and $(L_x, L_y, L_z) = (105, 50, 10)$.

provided the streaks are strong enough. This roughness-induced transition has been extensively investigated experimentally by different authors^{8,17}. For cylindrical roughness elements, in the early 60's, most of the results available back then have been reviewed in Ref.¹⁸ into one transition diagram, thus giving an empirical criterion for transition. However, fewer studies have been carried out on smooth roughness elements, and the influence of the shape of the roughness on the destabilisation process has not yet been investigated in detail. Though the mechanism responsible for transition to turbulence in the flow past a 3D roughness element is not yet fully understood, it is believed that it is due to an instability of the streaks induced by the roughness elements.

Following the theoretical work by Cossu & Brandt⁶, Fransson *et al.*^{11,10,12} have conducted a series of experiments demonstrating the ability for finite amplitude streaks to stabilise the Tollmien-Schlichting waves. With this aim, they have placed an array of roughness elements, having an aspect ratio $\eta = 3$, located at $x_k = 57.14$ from the leading edge of a flat plate and separated one from another by a spanwise distance $L_z = 10$ (Ref. 10). Despite the stabilising effect of the streaks on the TS waves, transition was however observed to take place right downstream the roughness elements beyond a critical Reynolds number. In this work, the case described in Ref. 10 is reproduced numerically, in order to show that fully three-dimensional global instability analysis is able to predict with reasonable accuracy the critical Reynolds number experimentally obtained by the previously mentioned authors and to provide a better understanding of the underlying physical mechanisms responsible for transition.

2. Problem formulation

2.1. Governing equations

The dynamics of a three-dimensional incompressible flow is described by the incompressible Navier-Stokes equations:

$$\begin{cases} \frac{\partial \mathbf{U}}{\partial t} + (\mathbf{U} \cdot \nabla) \mathbf{U} = -\nabla P + \frac{1}{Re} \Delta \mathbf{U} \\ \nabla \cdot \mathbf{U} = 0 \end{cases} \quad (1)$$

where $\mathbf{U} = (U, V, W)^T$ is the velocity vector and P the pressure term. Dimensionless variables are defined with respect to the height h of the cylindrical roughness element and the free-stream velocity U_∞ . Therefore, the Reynolds number is defined as $Re = U_\infty h / \nu$, with ν being the kinematic viscosity. Regarding the coordinate system, x , y and z are defined as the streamwise, wall-normal and spanwise directions, respectively, with x having its origin at the leading edge of the flat plate. However, since the domains used in this work do not include the leading edge of the flat plate, it is convenient to define a shifted streamwise axis $X = x - x_k$, having its origin at the location x_k of the roughness element along the flat plate. A sketch of the computational domain considered is depicted on figure 1, along with this roughness-centered coordinate system. The cylindrical roughness element, having diameter $d = 3$ and height $h = 1$,

is thus centred in $(X, z) = (0, 0)$. In the absence of the roughness element, the incoming Blasius boundary layer flow would be characterised by $Re_{\delta_s} = 281$ at $X = 0$ when the Reynolds number is set to $Re = 466$, and by $Re_{\delta_s} = 312$ for the highest Reynolds number considered herein, *i.e.* $Re = 575$. The computational box has a streamwise extent $L_X = 105$ ($-15 \leq X \leq 90$), a wall-normal extension of $L_y = 50$, and spanwise extent $L_z = 10$. The following boundary conditions have been applied:

- at the inlet ($X_{in} = -15$), a Dirichlet boundary condition is imposed on the velocity.
- at the outlet ($X_{out} = 90$), a Neumann boundary condition is imposed on the velocity $\nabla \mathbf{U} \cdot \mathbf{x} = 0$;
- on the spanwise end planes ($z_{side} = \pm L_z/2$), periodic boundary conditions are imposed for the three components of the velocity vector;
- at the upper boundary ($y_{top} = 50$), the following conditions are applied: $U = 1$ and $\partial V/\partial y = \partial W/\partial y = 0$;
- finally, a no-slip boundary condition is imposed on the flat plate and the walls of the roughness element.

Calculations have been performed using the code Nek5000 developed at Argonne National Laboratory by Fischer *et al.*⁹. Spatial discretisation is done by a Legendre spectral elements method with polynomials of order 12. Results presented herein have been obtained on the finest mesh used, *i.e.* 13 308 spectral elements resulting in approximately 2.3 millions gridpoints. The convective terms are advanced in time using an extrapolation of order 3, whereas for viscous terms a backward differentiation of order 3 is used, resulting in the time-advancement scheme labelled BDF3/EXT3.

2.2. Base flows computation

Base flows $\mathbf{U}_b = (U_b, V_b, W_b)^T$ have been computed using the selective frequency damping (SFD) approach introduced by Akervik *et al.*². This technique enables a damping of the oscillations of the unsteady part of the solution using a temporal low-pass filter. This is achieved by adding a forcing term to the right-hand side of the Navier-Stokes equations and extending the system (1) with an equation for the filtered state $\tilde{\mathbf{U}}$. The extended system is then governed by the following set of equations:

$$\begin{cases} \nabla \cdot \mathbf{U} = 0 \\ \frac{\partial \mathbf{U}}{\partial t} = -(\mathbf{U} \cdot \nabla) \mathbf{U} - \nabla P + \frac{1}{Re} \Delta \mathbf{U} - \chi(\mathbf{U} - \tilde{\mathbf{U}}) \\ \frac{\partial \tilde{\mathbf{U}}}{\partial t} = \omega_c(\mathbf{U} - \tilde{\mathbf{U}}) \end{cases} \quad (2)$$

with χ being the gain of the filter and ω_c its cutting circular frequency. The choice of these two parameters is crucial for the computation of unstable base flows: the parameter χ has to be positive and larger than the growth rate σ of the instability one aims to quench, whereas ω_c has to be lower than the eigenfrequency ω of the instability (usually $\omega_c = \omega/2$).

2.3. Three-dimensional stability analysis

Linear stability analysis enables the investigation of the asymptotic time evolution of infinitesimal perturbations in the vicinity of a given fixed point of the original system. The linearised dynamics of such infinitesimal perturbations evolving onto the base flow \mathbf{U}_b are governed by the linearised Navier-Stokes equations subject to the same boundary conditions as system (1) with the inlet Dirichlet boundary condition being a zero-velocity condition. Once projected onto a divergence-free vector space, these linearised equations simply read:

$$\frac{\partial \mathbf{u}}{\partial t} = \mathcal{A} \mathbf{u} \quad (3)$$

with \mathcal{A} being the projection of the Jacobian matrix onto the divergence-free vector space and $\mathbf{u} = (u, v, w)^T$ the perturbation velocity vector. Because the number of degrees of freedom involved in the computation is far too large to enable explicit storage of \mathcal{A} and thus direct computation of its eigenvalues, a time-stepper approach is used^{7,3}. This

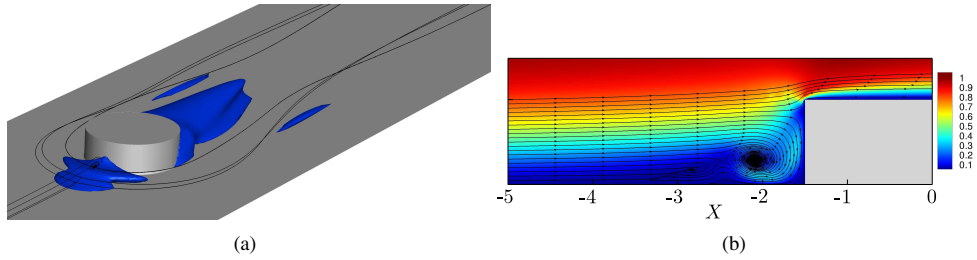


Fig. 2. Visualisations of the base flow for $(Re, Re_{\delta^*}) = (466, 281)$. (a) Visualisation of the vortical system using streamlines and isosurfaces of the upstream and downstream reversed flow regions (visualised by the $U_b = 0$ isosurface). (b) Close-up of the upstream vortical system highlighted by streamlines in the symmetry plane coloured with the velocity magnitude.

method, based on an Arnoldi factorisation and on the formal solution $\mathbf{u}(\Delta t) = e^{\mathcal{A}\Delta t}\mathbf{u}_0$ to equation (3), is aimed at computing the eigenpairs of the exponential propagator $\mathbf{M} = e^{\mathcal{A}\Delta t}$ instead of those of the Jacobian matrix \mathcal{A} . Indeed, though the Jacobian matrix \mathcal{A} cannot be explicitly computed, the action of the exponential propagator onto a given vector can be easily approximated by time-marching the linearised Navier-Stokes equations from $t = 0$ to $t = \Delta t$. At iteration k , the basic Arnoldi iteration thus reads:

$$\mathbf{M}\mathbf{V}_k \simeq \mathbf{V}_k\mathbf{H}_k \quad (4)$$

with \mathbf{V}_k being an orthonormal set of vectors spanning a Krylov subspace of dimension k onto which \mathbf{M} is projected, and \mathbf{H}_k the associated projection. The Hessenberg matrix \mathbf{H}_k resulting from this Arnoldi iteration is a small $k \times k$ matrix whose eigenpairs (Σ, \mathbf{X}) , also called Ritz pairs, can be directly computed and are a good approximation of those of \mathbf{M} . Ritz pairs are linked to the eigenvalues and eigenvectors (Λ, \mathbf{Q}) of the Jacobian matrix \mathcal{A} by the following relationship:

$$\Lambda = \frac{\log(\Sigma)}{\Delta t}, \quad \mathbf{Q} = \mathbf{V}\mathbf{X} \quad (5)$$

with $\Lambda = \sigma + i\omega$, σ being the growth rate and ω the circular frequency. All of the results presented throughout this paper were obtained using a Krylov subspace of dimension 500 and a sampling period $\Delta t = 0.625$ enabling good convergence of the eigenvalues with circular frequency equals to 2.5 and lower.

3. Results

3.1. Base flows

Figure 2 depicts the base flow obtained for $(Re, Re_{\delta^*}, \eta) = (466, 281, 3)$, i.e. the same setup as the reference one in Ref. 10. It exhibits the two major features of all the steady solutions that have been investigated within the present work: an upstream and a downstream reversed flow region (visualised by the $U_b = 0$ isosurface in the left frame), as well as a system of multiple vortices stemming from the upstream recirculation zone, wrapping around the roughness element and eventually getting almost aligned with the streamwise direction as shown by the streamlines. The topology of this upstream vortical system has been investigated experimentally by Baker⁴ and exhibits between one and three counter-rotating vortex pairs. According to Baker⁴, the particular vortical topology chosen by the flow essentially depends on the Reynolds number and on the ratio of the roughness element's diameter d over the boundary layer displacement thickness δ^* . This vortical system can be seen on figure 2(b) depicting streamlines in the symmetry plane. The impact of this vortical system on the boundary layer flow is as follows:

- (i) Upstream the roughness element, all of the vorticity is in the spanwise direction.
- (ii) When the flow encounters the roughness element, the upstream spanwise vorticity rolls up, forming the vortical system observed in figure 2(b).
- (iii) It then wraps around the roughness element and is transferred into streamwise vorticity further downstream thus creating the legs of the horseshoe vortices.

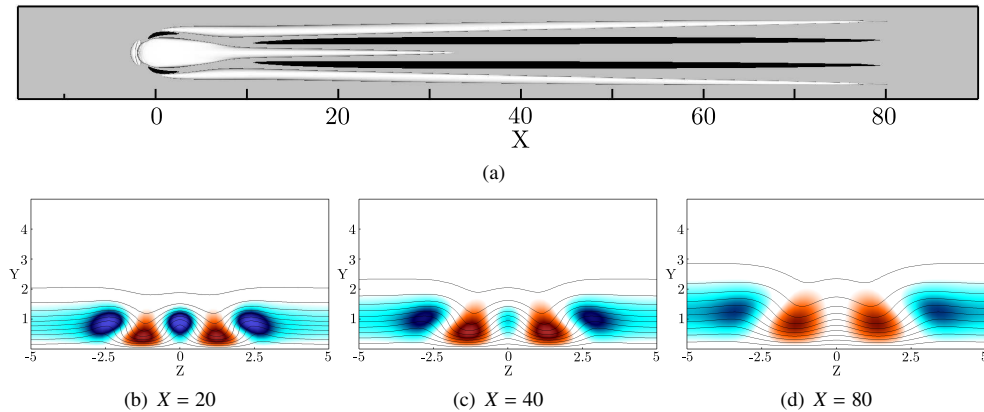


Fig. 3. Streamwise evolution of the streaks induced by the array of roughness elements for $(Re, Re_{\delta^*}) = (466, 281)$. Top view of $\bar{u} = \pm 0.3$ surfaces (black positive and white negative) with $\bar{u} = U_b - U_{Bl}$ being the deviation of the base flow from the Blasius boundary layer flow (a) ; slices extracted at $X = 20$ (b), $X = 40$ (c) and $X = 80$ (d). The shaded contours range from $\bar{u} = 0.3$ (red) to $\bar{u} = -0.3$ (blue), whereas the solid lines depict the base flows streamwise velocity isocontours from $U_b = 0.1$ to 0.99 .

The legs of these horseshoe vortices being streamwise-aligned vortices, high speed fluid is transported from the outer region of the boundary layer toward the wall, whereas low speed fluid is transported away from the wall toward the outer region of the boundary layer. This transport of momentum, known as the lift-up effect, thus gives birth to streamwise streaks¹⁵.

Figure 3 depicts the spatial distribution of the central low-speed region and outer streaks induced by the array of roughness elements at various streamwise stations. These streaks have been identified using the deviation of the base flow streamwise component from the corresponding Blasius boundary layer flow (U_{Bl}), as used by Fisher & Choudhari⁸, i.e. $\bar{u} = U_b - U_{Bl}$. As depicted on figure 3(a), the roughness element generates a central low-speed region created by the streamwise velocity deficit induced by the roughness element and a pair of high- and low-speed streaks on each side induced by the legs of the primary horseshoe vortex. On the one hand, the central low-speed region appears to fade away relatively rapidly in the streamwise direction, while on the other hand the outer pairs of streaks appear to sustain over quite a long distance. This can be better visualised on figures 3(b) to (d) depicting contours of the streamwise velocity deviation in various $X = \text{constant}$ planes. It indeed appears clearly from these figures that, while the amplitude of the central low-speed region has dramatically decreased as soon as $X = 40$, the amplitude of the outer low- and high-speed streaks varies very little. Such behavior has already been observed experimentally by Fransson *et al.*¹¹ (see figure 2 of the cited paper).

3.2. Linear stability

In order to investigate the early transition observed in the experiment described in Ref. 10, global stability analyses of various base flows are conducted. Figure 4 depicts the spectra of eigenvalues for $Re = 550$ ($Re_{\delta^*} = 305$) and $Re = 575$ ($Re_{\delta^*} = 319$). It is clear from these eigenspectra that the flow experiences a Hopf bifurcation for $550 < Re_c < 575$ due to an isolated pair of complex conjugate eigenvalues of the linearised Navier-Stokes operator moving into the upper-half complex plane. A linear interpolation provides a critical Reynolds number $Re_c = 564$ ($(Re_{\delta^*})_c = 309$) only 6% larger than the critical Reynolds number experimentally obtained in Ref. 10. This good agreement for the value of the critical Reynolds number strongly suggests that the transition observed in the experiment might be the consequence of a three-dimensional global instability of the flow.

The shape of the associated unstable global mode is depicted on figure 5. As one can see on figure 5(a), this mode takes the form of streamwise alternated patches of positive and negative velocity exhibiting a varicose symmetry with respect to the spanwise mid-plane. To get a better insight of the structure of the mode and of its location with respect to the base flow's features, figure 5 provides slices of its spatial support in the $X = 23$ (b) and the $X = 40$ (c) plane. The

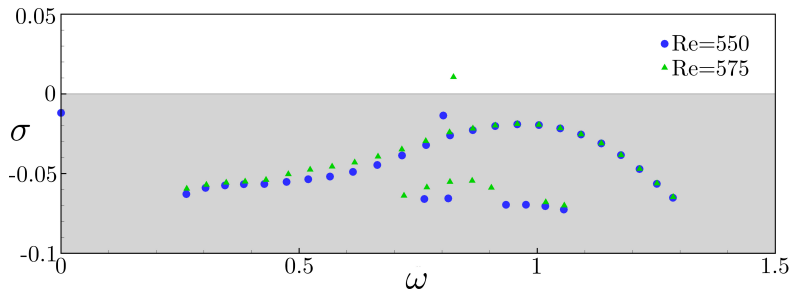


Fig. 4. Eigenspectrum of the linearised Navier-Stokes operator. Blue dots show the eigenvalues for $(Re, Re_{\delta^*}) = (550, 305)$, whereas green triangles show the one for $(Re, Re_{\delta^*}) = (575, 312)$.

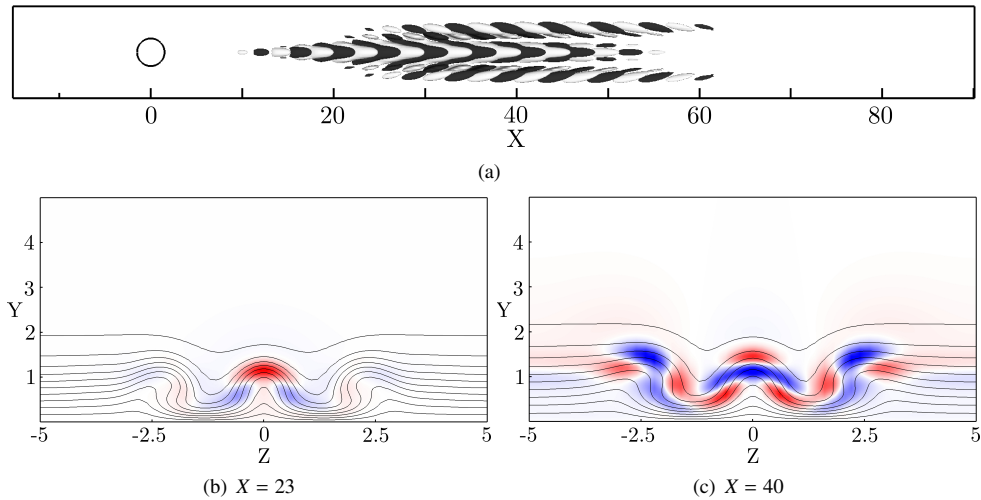


Fig. 5. Visualisation of the streamwise velocity component of the leading unstable mode at $(Re, Re_{\delta^*}) = (575, 312)$. (a) Top view of isosurfaces depicting $\pm 10\%$ of the mode's maximum streamwise velocity. (b) and (c) depict slices of the mode in the $X = 23$ and $X = 40$ planes, respectively. In both figures, the colormap has been normalised by the local maximum velocity. The solid lines depict the base flows streamwise velocity isocontours from $U_b = 0.1$ to 0.99 .

mode is identified using its streamwise velocity contours (shaded) whereas the solid black lines depict the baseflow U_b isocontours. These figures make it clear that, though the mode is initially located along the central low-speed region, it then contaminates almost the whole spanwise extent of the domain before fading away for $X > 60$. Moreover, for all of the streamwise planes considered, the maximum of the mode is located along the shear layers delimiting the central low-speed region and the streaks.

3.3. Instability mechanisms

3.3.1. Perturbation kinetic energy budget

Aiming to get a better understanding of the mechanisms yielding the flow to become unstable and to understand how and where this varicose unstable global mode extracts its energy, the transfer of kinetic energy between the base flow and the unstable mode is investigated. Similar analysis has already been conducted in a local framework by Brandt⁵. Calculating this kinetic energy transfer has proven to be very helpful in order to get a better insight of the instability mechanisms. The kinetic energy rate of change is given by the Reynolds-Orr equation:

$$\frac{\partial E}{\partial t} = -D + \sum_{i=1}^9 \int_V I_i dV \quad (6)$$

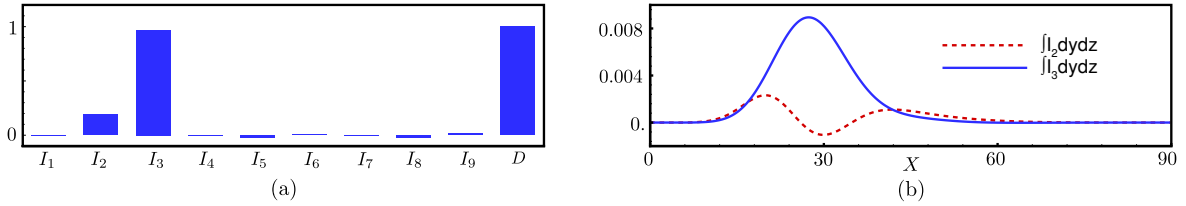


Fig. 6. (a) Kinetic energy budget integrated over the whole domain. (b) Streamwise evolution of the production terms $\int_V I_2 dydz$ (red dashed line) and $\int_V I_3 dydz$ (blue solid line).

where the total kinetic energy and the total dissipation in the computational domain's volume V are given by:

$$E = \frac{1}{2} \int_V \mathbf{u} \cdot \mathbf{u} dV, \quad D = \frac{1}{Re} \int_V \nabla \mathbf{u} : \nabla \mathbf{u} dV \quad (7)$$

and where the integrands I_i which represent the production terms are:

$$\begin{aligned} I_1 &= -u^2 \frac{\partial U_b}{\partial x}, \quad I_2 = -uv \frac{\partial U_b}{\partial y}, \quad I_3 = -uw \frac{\partial U_b}{\partial z} \\ I_4 &= -uv \frac{\partial V_b}{\partial x}, \quad I_5 = -v^2 \frac{\partial V_b}{\partial y}, \quad I_6 = -vw \frac{\partial V_b}{\partial z} \\ I_7 &= -wu \frac{\partial W_b}{\partial x}, \quad I_8 = -wv \frac{\partial W_b}{\partial y}, \quad I_9 = -w^2 \frac{\partial W_b}{\partial z} \end{aligned} \quad (8)$$

The sign of the different integrands I_i indicates whether the local transfer of kinetic energy associated to them acts as stabilising (negative) or destabilising (positive). For the sake of comparison, all the kinetic energy budgets presented in this section have been normalised by the dissipation D .

Results of this kinetic energy analysis are summarised in figures 6 for $Re = 575$. At this Reynolds number, a slightly super-critical one, one can see on figure 6(a) that, though $\int_V I_2 dV$ gives a small non-zero contribution to the energy extraction process, the mode surprisingly extracts most of its energy from the work of uw against the spanwise gradient of the base flow streamwise component $\partial U_b / \partial z$, whereas in a local framework, varicose modes are usually linked to the transport of the wall-normal gradient. Looking at the streamwise evolution of these two terms depicted on figure 6(b) helps us to understand this surprising dominance of $\int_V I_3 dV$. Indeed, whereas $\int_{y,z} I_3 dydz$ is positive throughout the whole streamwise extent of the domain, one can see that $\int_{y,z} I_2 dydz$ has a smaller amplitude and even acts as slightly stabilising in a portion of the computational domain (from $X \simeq 25$ up to $X \simeq 40$). This can be explained by the features of the associated base flow: while the spanwise gradient remains more or less constant throughout the computational domain, the destabilising effect of the wall-normal gradient induced by the central low-speed region quickly drops as the central low-speed region starts to fade away beyond $X \simeq 30$.

Figures 7(a) and (b) provide the spatial distribution of the I_2 and I_3 integrands in the streamwise $X = 25$ plane. This varicose unstable mode seems to extract its energy from the fully three-dimensional shear layer as a whole. More importantly, most of its energy is extracted along the streaks relatively far downstream the roughness element as highlighted by the curves on figures 6(b) as well as on the spatial distribution of the I_3 term in an horizontal plane as shown on figure 7(c).

3.3.2. Wavemaker

Investigating the perturbation kinetic energy budget has proven helpful to get a better understanding of the instability mechanisms. Yet, such analysis provides only limited information about the core region of the instability, i.e. the region known as the wavemaker. The concept of wavemaker has been introduced by Giannetti & Luchini¹³ and Marquet *et al.*¹⁶ where it has been illustrated on the global instability of the two-dimensional cylinder flow. It enables

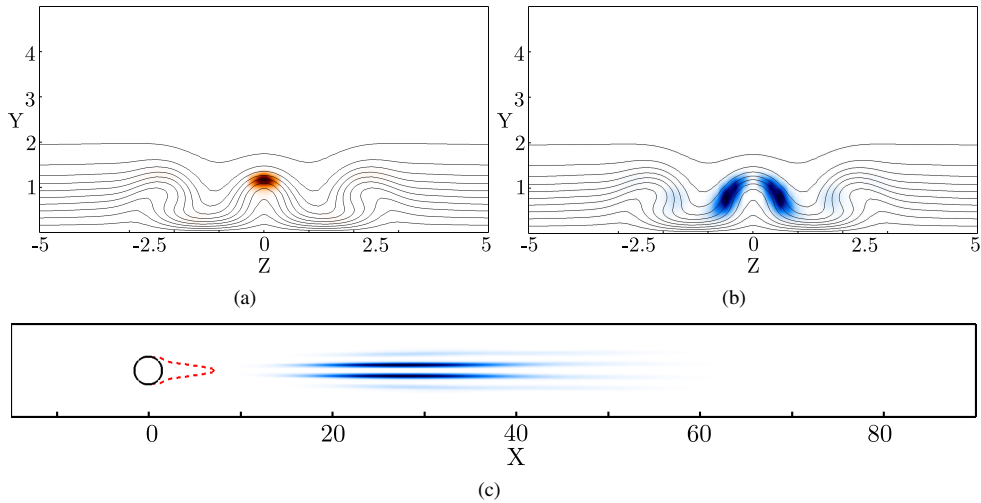


Fig. 7. Top: Spatial distribution of the $I_2 = -uv\partial U_b/\partial y$ (a) and $I_3 = -uw\partial U_b/\partial z$ (b) production terms in the plane $X = 25$. Solid lines depict the base flows streamwise velocity isocontours from $U_b = 0.1$ to 0.99 . (c) Spatial distribution of I_3 in the $y = 0.75$ horizontal plane. Red dashed line depicts the spatial extent of the downstream reversed flow region.

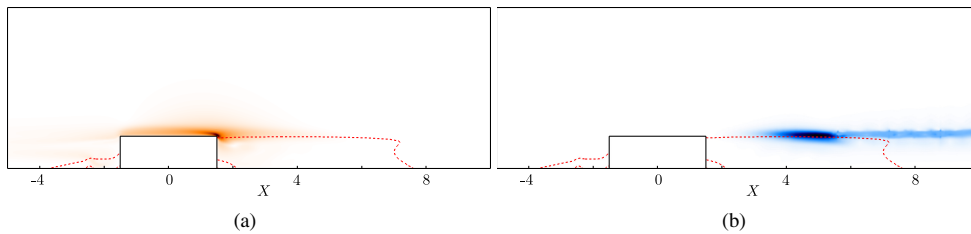


Fig. 8. (a) Norm of the leading adjoint mode and (b) the wavemaker in the $z = 0$ symmetry plane. The red dashed line depicts the spatial extent of the reversed flow regions.

one to identify the most likely region for the inception of the global instability under consideration. Following the definition given in Ref. 13, the wavemaker is given as the overlap of the direct and adjoint modes:

$$\zeta(x, y, z) = \frac{\|\mathbf{u}(x, y, z)\| \|\mathbf{u}^\dagger(x, y, z)\|}{\langle \mathbf{u}^\dagger, \mathbf{u} \rangle} \quad (9)$$

where \mathbf{u}^\dagger is the adjoint of the global mode considered (see figure 8(a)). The wavemaker of the unstable mode considered herein is depicted on figure 8(b). It is clear from figure 8 that this wavemaker has an elongated spatial support. Indeed, not only is it localised within the downstream reversed flow region but it also extends along the top of the central low-speed region. This spatial extent further highlights the key role of the central low-speed region and outer streaks on this instability. However, despite its elongated nature, it is worthy to note that the amplitude of the varicose wavemaker within the downstream reversed flow region still is almost ten to fifteen times larger than that within the wake of the roughness element. From these elements, it thus appears that:

- (i) This varicose mode finds its roots in a global instability of the downstream reversed flow region. However, based on the kinetic energy budget, this particular region appears to behave essentially as a wave generator and plays very little role in the energy extraction process of the instability.
- (ii) Once generated from the wavemaker, the varicose global mode then experiences large spatial transient growth along the central low-speed region induced by the roughness element that dominates the whole energy budget.

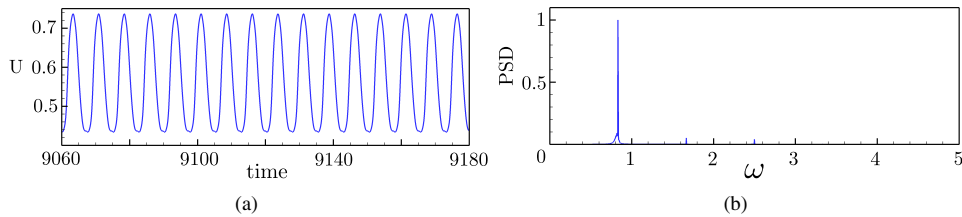


Fig. 9. Probe measurements and normalised Fourier spectrum of the streamwise velocity in the near wake region at $(X, y, z) = (10, 0.5, 0)$ and at a Reynolds number $Re = 575$.

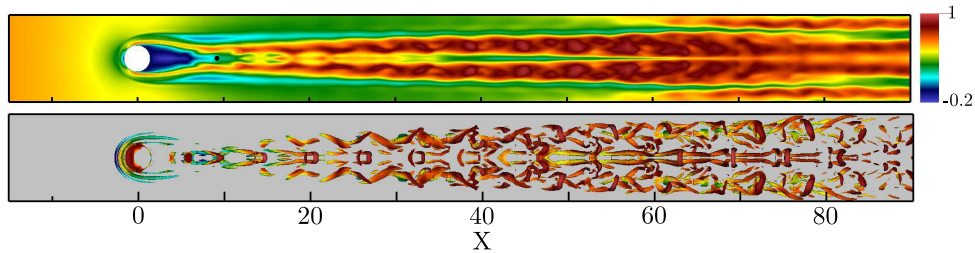


Fig. 10. Top: Instantaneous streamwise velocity distribution in the $y = 0.5$ plane. The black dot depicts the location of the probe used to record the data shown in figure 9. Bottom: Top view of the hairpin vortices using isosurfaces of $\lambda_2 = -0.025$ coloured with local kinetic energy of the flow.

As will be shown in section 3.4, such varicose instability non-linearly seems to give rise to hairpin vortices shed directly from the roughness element. It thus appears that the linear mechanism identified from the perturbation kinetic energy and wavemaker analyses of this varicose global instability is similar to the one proposed by Acarlar & Smith¹ for the creation of hairpin vortices right downstream a hemispheric protuberance, i.e. a small roll-up of the downstream shear layer that is then convected by the flow and greatly amplified along the central-low speed region, eventually giving birth to a hairpin vortex due to non-linear effects.

3.4. Non-linear evolution

In order to have a glimpse of the non-linear evolution of the varicose global instability identified previously, a direct numerical simulation (DNS) is conducted for $Re = 575$, for which the global stability analysis of the base flow predicts that only a single varicose global mode is unstable. The non-linear Navier-Stokes equations have been initialised using the base flow solution and are marched in time until a statistically steady state has been reached. Figure 9(a) shows the streamwise velocity signal recorded by a probe located at $(X, y, z) = (10, 0.5, 0)$, while figure 9(b) presents the associated Fourier spectrum. It is clear from figure 9(a) that the dynamics of the flow exhibits well established periodic oscillations. As shown in figure 9(b), these oscillations of the flow have a circular frequency $\omega_{DNS} = 0.832$, very close to that of the unstable varicose global mode identified in section 3.2 (i.e. $\omega = 0.824$). Figure 10 depicts instantaneous vortical structures present within the flow that have been identified using the λ_2 criterion¹⁴. It seems obvious from this figure that these vortical structures are hairpin vortices shed directly downstream the roughness element. It thus appears that the self-sustaining oscillations of the flow recorded by the probe consist in a periodic shedding of hairpin vortices resulting in a varicose modulation of the central low-speed region and surrounding velocity streaks as shown on figure 10(b). Moreover, it can be assessed from the large population of hairpin vortices that transition is triggered very close to the roughness element, coherent with the numerous experimental observations reviewed by von Doenhoff & Braslow¹⁸. Based on these observations and on results from global stability analyses, one can conclude that the unstable varicose global mode contributes to the birth of the set of hairpin vortices non-linearly generated and might thus explain the early transition observed in the experimental work by Fransson *et al.*¹⁰ for supercritical Reynolds numbers.

4. Summary & conclusions

The properties of the incompressible flow induced by a three-dimensional cylindrical roughness element of aspect ratio $\eta = 3$ has been investigated by the joint application of three-dimensional stability analyses and direct numerical simulations. Horseshoe vortices are created around the roughness element, whose legs create two pairs of high- and low-speed streamwise streaks due to the lift-up effect. Furthermore, a central low-speed region, whose crucial importance in the transition process has been indicated by several authors, as well as in the present work, is created due to the streamwise velocity blockage induced by the presence of the roughness element. The strength of this central low-speed region, and whether or not it sustains over a long streamwise distance, is closely linked both to the roughness element's aspect ratio and to the Reynolds number.

Regarding the stability of such flows, a varicose global instability of the flow has been identified. The underlying physical mechanisms are investigated by means of a kinetic energy transfer analysis between the base flow and the perturbations as well as by the computation of the wavemaker. This varicose mode appears to be related to a global instability of the whole three-dimensional shear layer surrounding the central low-speed streak. In particular, a weak pocket of instability is originated in the near wake, which is strongly amplified further downstream due to the highly convective nature of the downstream flow similarly to the explanation proposed by Acarlar & Smith¹ regarding the creation of hairpin vortices right downstream hemispheric roughness elements.

Non-linear direct numerical simulations have revealed that this varicose global instability of the flow gives rise to a shedding of hairpin vortices right downstream the roughness elements. These hairpin vortices trigger a very rapid transition of the flow right after the roughness elements. Despite the transitional dynamics, Fourier analysis has shown that the dominant frequency involved in the dynamics are in good agreement with the predictions made by global stability analysis.

References

1. M. Acarlar and C. Smith. A study of hairpin vortices in a laminar boundary layer: part I, hairpin vortices generated by a hemisphere protuberance. *J. Fluid Mech.*, 175:1–41, 1987.
2. E. Akervik, L. Brandt, D.S. Henningson, J. Hoepffner, O. Marxen, and P. Schlatter. Steady solutions of the Navier-Stokes equations by selective frequency damping. *Phys. Fluids*, 18(068102), 2006.
3. S. Bagheri, E. Akervik, L. Brandt, and D.S. Henningson. Matrix-free methods for the stability and control of boundary layers. *AIAA Journal*, 47(5):1057–1068, 2009.
4. C. J. Baker. The laminar horseshoe vortex. *J. Fluid Mech.*, 95:347–367, 1978.
5. L. Brandt. Numerical studies of the instability and breakdown of a boundary-layer low-speed streak. *European Journal of Mechanics - B/Fluids*, 26(1):64–82, 2007.
6. C. Cossu and L. Brandt. On Tollmien-Schlichting-like waves in streaky boundary layers. *European Journal of Mechanics - B/Fluids*, 23(6):815–833, 2004.
7. W.S. Edwards, L.S. Tuckerman, R.A. Friesner, and D.C. Sorensen. Krylov methods for the incompressible Navier-Stokes equations. *Journal of Computational Physics*, 110:82–102, 1994.
8. P. Fischer and M. Choudhari. Numerical simulation of roughness induced transient growth in a laminar boundary layer. In *34th AIAA Fluid Dynamics Conference*, 2004.
9. P.F. Fischer, J.W. Lottes, and S.G. Kerkemeir. nek5000 Web pages, 2008. <http://nek5000.mcs.anl.gov>.
10. J. H. Fransson, L. Brandt, A. Talamelli, and C. Cossu. Experimental study of the stabilization of tollmien-schlichting waves by finite amplitude streaks. *Phys. Fluids*, 17(054110), 2005.
11. J.H.M. Fransson, L. Brandt, A. Talamelli, and C. Cossu. Experimental and theoretical investigation of the nonmodal growth of steady streaks in a flat plate boundary layer. *Physics of Fluids*, 10(3627), 2004.
12. J.H.M. Fransson, A. Talamelli, L. Brandt, and C. Cossu. Delaying transition to turbulence by a passive mechanism. *Phys. Rev. Letters*, 96(064501), 2006.
13. F. Giannetti and P. Luchini. Structural sensitivity of the first instability of the cylinder wake. *J. Fluid Mech.*, 581:167–197, 2007.
14. J. Jeong and F. Hussain. On the identification of a vortex. *J. Fluid Mech.*, 285:69–94, 1995.
15. M.T. Landahl. On sublayer streaks. *J. Fluid Mech.*, 212:593–614, 1990.
16. O. Marquet, D. Sipp, and L. Jacquin. Sensitivity analysis and passive control of cylinder flow. *J. Fluid Mech.*, 615:221–252, 2008.
17. I. Tani, H. Komoda, and Y. Komatsu. Boundary-layer transition by isolated roughness. Technical Report 375, Aeronautical Research Institute, University of Tokyo, 1962.
18. A.E. von Doenhoff and A.L. Braslow. The effect of distributed roughness on laminar flow. In Lachmann, editor, *Boundary layer control*, volume 2. Pergamon, 1961.